



# Near-field radiative heat transfer with doped-silicon nanostructured metamaterials



X.L. Liu, R.Z. Zhang, Z.M. Zhang\*

George W. Woodruff School of Mechanical Engineering, Georgia Institute of Technology, Atlanta, GA 30332, USA

## ARTICLE INFO

### Article history:

Received 24 September 2013  
Received in revised form 10 January 2014  
Accepted 10 February 2014  
Available online 14 March 2014

### Keywords:

Effective medium theory  
Hyperbolic metamaterials  
Nanostructures  
Near-field thermal radiation

## ABSTRACT

The objective of this work is to evaluate different practically achievable doped-silicon (D-Si) nanostructured metamaterials (including nanowires and nanoholes, multilayers, and one-dimensional gratings) in terms of their potential for enhancing near-field radiative heat transfer at ambient temperature. It is found that both doped silicon nanowires and nanoholes may achieve an enhancement over bulk doped silicon by more than one order of magnitude in the deep submicron gap region. The enhancement is attributed to either the broadband hyperbolic modes or low-loss surface modes or a combination of both. On the other hand, polarization coupling, which can occur in the grating configuration, contributes little to the radiative transfer at the nanometer scale. This work will facilitate the application of nanostructures in more efficient non-contact thermal management, thermal imaging, and near-field thermophotovoltaics.

© 2014 Elsevier Ltd. All rights reserved.

## 1. Introduction

Near-field radiative heat transfer has attracted significant attention in recent years due to its wide potential applications in micro-scale thermophotovoltaic (TPV) cells [1–8], submicron thermal imaging [9–12], non-contact thermal rectifiers [13–16], thermal modulators [17–19], and local thermal management [20–22]. Planck's law of blackbody radiation breaks down when two objects at different temperatures are placed close enough, i.e., at a distance close to or smaller than the characteristic wavelength of thermal radiation [23–25]. At nanometer distances, near-field radiative heat transfer could be orders of magnitude greater than that between two blackbodies, especially when surface plasmon polaritons (SPPs) or surface phonon polaritons (SPhPs) are excited [26–29]. A number of groups have experimentally demonstrated that near-field radiation can exceed the blackbody limit using plate-plate or sphere-plate geometries [30–35].

Large heat transfer coefficients are desired for increased power throughput or heat dissipation in energy harvesting [4] or cooling [20] applications, respectively. However, the super-Planckian thermal radiation enabled by surface modes (either SPPs or SPhPs) is

usually narrowband and has high loss due to the inherent resonance effects, thus precluding more efficient heat transport. Reducing material loss (e.g., by reducing the electron scattering rate) could increase the cutoff wavevector and thus helps to improve near-field heat transfer [27,36]. Another method to obtain higher radiative heat flux is to broaden the super-Planckian radiation band with the help of the resonance-free hyperbolic modes [37–41]. Hyperbolic dispersion or hyperbolic modes may exist in natural or artificial anisotropic materials in certain frequency regions, where the electromagnetic waves with large transverse wavevector can propagate inside the hyperbolic metamaterials, unlike surface modes where the electromagnetic waves propagate only along the interface and decay into both media. Hyperbolic metamaterials, no matter whether they exist in nature (such as graphite) or are artificially synthesized, exhibit hyperbolic dispersion only in certain frequency ranges and are not ideally lossless [38–42]. Therefore, achieving a great enhancement of near-field radiative thermal transport beyond bulks for more efficient thermal transport or heat dissipation is still a challenge.

Doped silicon (D-Si) has been shown to support surface modes in the infrared spectrum and can enhance near-field radiative transfer [23,27,29,43] to similar magnitude as those for SiC and SiO<sub>2</sub> based on narrowband phonon modes [44]. Furthermore, the doping level can be varied to tune the far-field radiative properties [45] or near-field heat transfer [46]. Recent studies have shown that doped Si nanowires can enhance near-field radiation over bulk by several times [47]. Additionally, doped Si nanowires can exhibit

\* Corresponding author. Address: George W. Woodruff School of Mechanical Engineering, 801 Ferst Drive, NW, Georgia Institute of Technology, Atlanta, GA 30332-0405, USA. Tel.: +1 (404) 385 4225; fax: +1 (404) 894 8496.

E-mail address: [zhuomin.zhang@me.gatech.edu](mailto:zhuomin.zhang@me.gatech.edu) (Z.M. Zhang).

URL: <http://www.me.gatech.edu/~zzhang> (Z.M. Zhang).

### Nomenclature

$c$	speed of light in vacuum
$\mathbf{D}$	matrix
$d$	gap distance, m
$f$	volume filling ratio of D-Si
$h$	heat transfer coefficient, W/m <sup>2</sup> K
$\hbar$	reduced Planck constant, J s
$\mathbf{I}$	unit matrix
$i$	$\sqrt{-1}$
$k$	wavevector, m <sup>-1</sup>
$k_0$	wavevector in vacuum, m <sup>-1</sup>
$k_B$	Boltzmann constant, J/K
$n$	complex refractive index
$\mathbf{R}$	matrix formed by reflection coefficients
$r$	Fresnel's reflection coefficient
$T$	temperature, K

### Greek symbols

$\beta$	transverse wavevector, m <sup>-1</sup>
$\Delta$	relative rotation angle between the gratings, rad

$\varepsilon$	dielectric function
$\lambda$	wavelength, m
$\xi$	energy transmission coefficient or transmission factor
$\sigma$	Stefan-Boltzmann constant, W/m <sup>2</sup> K <sup>4</sup>
$\phi$	azimuthal angle, rad
$\omega$	angular frequency, rad/s
$\omega_m$	surface plasmon frequency, rad/s

### Subscripts

E	extraordinary wave
O	ordinary wave
p	p polarization or TM wave
s	s polarization or TE wave

hyperbolic modes and support negative refraction in a broad frequency range [48]. Different techniques have been successfully demonstrated to create controlled silicon nanostructures [49,50]. It is envisioned that D-Si nanostructures may allow near-field radiative heat transfer to be significantly enhanced by enabling hyperbolic modes or by reducing loss for surface modes.

Four practically achievable nanostructures based on D-Si are considered here, namely, nanowires, nanoholes, multilayers, and one-dimensional (1D) gratings. Fluctuation–dissipation theorem is used to calculate the near-field and far-field radiative transfer, assuming that the nanostructures can be treated as an effective homogeneous medium with anisotropy. The mechanisms of enhancement or reduction of radiative transfer are elucidated by considering the frequency- and wavevector-dependent energy transmission factor.

## 2. Theoretical formulation

The schematics of doped-silicon nanowires (D-SiNWs), doped silicon nanoholes (D-SiNHs), multilayered metamaterials, and 1D gratings are shown in Fig. 1, where the  $x$  and  $y$  directions are assumed to extend to infinity and each medium is assumed to be semi-infinite. Both the multilayer and 1D grating structures are composed of D-Si and germanium (Ge), while nanowire and nanohole D-Si configurations are surrounded by vacuum. The filling ratio  $f$  for all aforementioned four different nanostructures is defined based on the volume fraction of D-Si, and  $d$  is the gap distance. Note that the minimum  $f$  for aligned D-SiNHs is  $(1 - \pi/4)$ , and the maximum  $f$  for aligned D-SiNWs is  $\pi/4$ , due to the geometrical limitations of the circular holes and wires, assuming the 2D lattice to be square. The dielectric function of D-Si is governed by the Drude model and can be obtained from Basu et al. [51]. The dielectric function of Ge is largely independent of wavelength in the infrared region, and can be approximated as a constant with  $\varepsilon_{\text{Ge}} = 16$ . Local effective medium theory (LEMT) is used to obtain the anisotropic dielectric function and is combined with fluctuation electrodynamics to calculate the near-field radiative heat transfer coefficient due to its simplicity and low computational demand [17,36–42,47,52]. The aforementioned nanostructures are treated as homogenous uniaxial materials; this assumption is valid in the far field as long as the characteristic thermal wavelength is

much greater than the nanostructure period. In the near field, as pointed out by some investigators, nonlocal effects would arise at the resonance frequency of surface plasmon polaritons (SPPs) or very large wavevectors [39,53,54]. Nevertheless, when the gap distance is much greater than the period of nanostructures, LEMT should be applicable in the near field as well [36]. In the present study, the period of nanostructures is assumed to be sufficiently small, so that LEMT can be applied to both the far and near fields.

In the Maxwell–Garnett theory, the effective properties of a composite medium are obtained by treating one constituent of the composite as the host and all other constituents as embedded grains (fillers), which are not in contact with one another. For D-SiNWs, vacuum is treated as the host with D-Si as the filler. For D-SiNHs on the other hand, D-Si is the host. When the electric field is along the optical axis ( $z$  direction), the dielectric function for both nanowires and nanoholes is given as

$$\varepsilon_z = 1 - f + \varepsilon_{\text{D-Si}} f \quad (1)$$

Here,  $\varepsilon_z$  is essentially governed by a diluted Drude model, since it is just the weighted average of the dielectric functions of doped silicon and vacuum. Note that Eq. (1) can be obtained from different effective medium approximations and should be valid for any  $f$  [47]. The Drude model of D-Si may be written as  $\varepsilon(\omega) = \varepsilon_\infty - \omega_p^2 / (\omega^2 + i\gamma\omega)$ , where  $\varepsilon_\infty$  is a high-frequency constant,  $\omega_p$  is the plasma frequency, and  $\gamma$  is the scattering rate [51]. The plasma frequency for D-SiNWs is  $\sqrt{f}$  times that of D-Si; and the high-frequency term for D-SiNWs is  $(1 - f + f\varepsilon_\infty)$ , which varies from 1 for  $f = 0$  to  $\varepsilon_\infty$  for  $f = 1$ . When the electric field is perpendicular to the optical axis, the ordinary dielectric function  $\varepsilon_x$ , which is equal to  $\varepsilon_y$ , of nanowires is governed by [45]

$$\varepsilon_{x,\text{NW}} = \frac{\varepsilon_{\text{D-Si}} + 1 + (\varepsilon_{\text{D-Si}} - 1)f}{\varepsilon_{\text{D-Si}} + 1 - (\varepsilon_{\text{D-Si}} - 1)f} \quad (2)$$

Note that  $\varepsilon_{x,\text{NW}}$  given above can be expressed as a Lorentz model, and detailed derivations can be found from [45]. From a physical point of view, it is because the free electrons in nanowires are bounded by surrounding vacuum [48]. It is assumed that Eq. (2) is applicable to any  $f$  until it reaches the maximum limit of  $\pi/4$ , when the diameter of the Si wire is the same as the period of the unit cell. This is a reasonable assumption as long as the Si wires are separated from each other. For nanoholes, Si should be treated as the host and

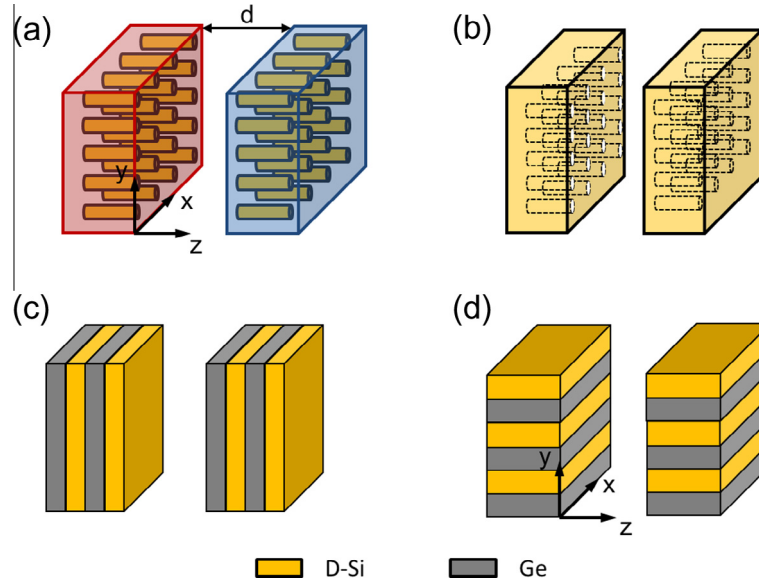


**Fig. 1.** Schematics of two semi-infinite nanostructured metamaterials separated by a vacuum gap at a distance  $d$ : (a) D-SiNWs; (b) D-SiNHs; (c) multilayers composed of D-Si and Ge, which is modeled as a dielectric; (d) 1D gratings composed of D-Si and Ge, where one of the gratings may be rotated about the  $z$  axis at an angle  $\Delta$ , although not shown in the figure. It is assumed that the space not occupied by Si in the nanowire and nanohole structures is evacuated.

the vacuum holes should be treated as the filler. In this case,  $\epsilon_{x,NH}$  can be calculated from the Maxwell–Garnett theory as follows

$$\epsilon_{x,NH} = \epsilon_{D-Si} \frac{\epsilon_{D-Si} f + (2 - f)}{\epsilon_{D-Si} (2 - f) + f} \quad (3)$$

Unlike in the case of nanowires,  $\epsilon_{x,NH}$  is dominated by a modified Drude model prescribed by Eq. (3), because free electrons in the nanohole structure are not bounded due to the interconnected doped silicon material.

The dielectric functions of the D-Si/Ge multilayer in orthogonal directions are given by

$$\epsilon_o = \epsilon_{Ge}(1 - f) + \epsilon_{D-Si} f \quad (4a)$$

$$\epsilon_e = \frac{\epsilon_{Ge} \epsilon_{D-Si}}{(1 - f) \epsilon_{D-Si} + \epsilon_{Ge} f} \quad (4b)$$

Here,  $\epsilon_o$  (ordinary) and  $\epsilon_e$  (extraordinary) are the dielectric functions for electric field perpendicular and along the optical axis, respectively. Note that for the multilayer configuration,  $\epsilon_x = \epsilon_y = \epsilon_o$  and  $\epsilon_z = \epsilon_e$ . The above dielectric functions also apply to 1D gratings but with  $\epsilon_z = \epsilon_o$  instead. In addition, the values of  $\epsilon_x$  and  $\epsilon_y$  for the grating depend on its rotation. In the aligned case as shown in Fig. 1d,  $\epsilon_x = \epsilon_o$  and  $\epsilon_y = \epsilon_e$ . It should also be noted that for the multilayered structure, both the Maxwell–Garnett and Bruggeman effective medium approaches give the same expressions, i.e., Eqs. (4a) and (4b). Detailed discussions of the effective medium approximations can be found from Refs. [55,56].

The heat transfer coefficient at temperature  $T$  between two anisotropic planar media separated by a vacuum gap  $d$  can be calculated from Biëhs et al. [38]

$$h = \frac{1}{8\pi^3} \int_0^\infty g(\omega, T) d\omega \int_0^{2\pi} \int_0^\infty \xi(\omega, \beta, \phi) \beta d\beta d\phi \quad (5)$$

where

$$g(\omega, T) = \frac{\partial}{\partial T} \left( \frac{\hbar\omega}{e^{\hbar\omega/k_B T} - 1} \right) = \frac{(\hbar\omega)^2 e^{\hbar\omega/k_B T}}{k_B T^2 (e^{\hbar\omega/k_B T} - 1)^2} \quad (6)$$

and  $\xi(\omega, \beta, \phi)$  is called the energy transmission coefficient or transmission factor (to distinguish from Fresnel’s transmission coefficient

which is based on the field). The transmission factor can be expressed in a matrix formulation as [36]

$$\xi(\omega, \beta, \phi) = \begin{cases} \text{Tr}[(\mathbf{I} - \mathbf{R}_2^* \mathbf{R}_2) \mathbf{D} (\mathbf{I} - \mathbf{R}_1 \mathbf{R}_1^*) \mathbf{D}^*], & \beta < k_0 \\ \text{Tr}[(\mathbf{R}_2^* - \mathbf{R}_2) \mathbf{D} (\mathbf{R}_1 - \mathbf{R}_1^*) \mathbf{D}^*] e^{-2|k_{z0}|d}, & \beta > k_0 \end{cases} \quad (7)$$

where  $k_0 = \omega/c$  is the wavevector in vacuum with  $c$  being the speed of light in vacuum,  $\beta$  is the transverse wavevector (i.e., the magnitude of the wavevector in the  $x$ - $y$  plane),  $k_{z0} = \sqrt{k_0^2 - \beta^2}$  is the wavevector component in the  $z$  direction in vacuum. Note that the symbol  $*$  denotes the conjugate transpose (Hermitian transpose), and  $\text{Tr}$  stands for trace.

In Eq. (7),  $\mathbf{I}$  is a  $2 \times 2$  unit matrix, and

$$\mathbf{R}_{1,2} = \begin{bmatrix} r_{ss}^{(1,2)} & r_{sp}^{(1,2)} \\ r_{ps}^{(1,2)} & r_{pp}^{(1,2)} \end{bmatrix} \quad (8a)$$

is the matrix that includes Fresnel’s reflection coefficients for incident from vacuum to medium 1 or 2, respectively. The matrix  $\mathbf{D}$  in Eq. (7) is determined by

$$\mathbf{D} = (\mathbf{I} - \mathbf{R}_1 \mathbf{R}_2 e^{2ik_{z0}d})^{-1} \quad (8b)$$

where “ $-1$ ” signifies an inverse matrix [17]. In the far field, the integration of Eq. (5) over  $\beta$  from 0 to  $k_0$  and over the azimuthal angle  $\phi$  from 0 to  $2\pi$  is essentially the hemispherical integration. However, in the near field, evanescent waves dominate the energy transfer since the transmission factor is nontrivial at large  $\beta$  values.

For an anisotropic medium, cross-polarization can exist and, in general,  $r_{sp} \neq 0$  and  $r_{ps} \neq 0$ . For aligned nanowires, nanoholes, and multilayer structures, the optical axis is in the  $z$  direction; subsequently,  $r_{sp} = r_{ps} = 0$ . Thus, the transmission factor  $\xi$  is independent of the azimuthal angle and can be written as  $\xi(\omega, \beta, \phi) = \xi_s(\omega, \beta) + \xi_p(\omega, \beta)$ , where [24,44]

$$\xi_j(\omega, \beta) = \begin{cases} (1 - |r_j|^2)^2 / |1 - r_j^2 e^{2ik_{z0}d}|^2, & \beta < k_0 \\ 4[\text{Im}(r_j)]^2 e^{-2|k_{z0}|d} / |1 - r_j^2 e^{2ik_{z0}d}|^2, & \beta > k_0 \end{cases} \quad (9)$$

Here,  $j$  is for s or p polarization, and  $\text{Im}$  denotes the imaginary part. It should be noted that for a single polarization, the transmission

factor is from 0 to 1. For s-polarized waves, the refraction in the uniaxial material is the same as in an isotropic medium with ordinary properties, since the electric field is perpendicular to the optical axis ( $z$  direction). Therefore, the s-polarization Fresnel coefficient  $r_s$  becomes [36,37]

$$r_s = \frac{k_{z0} - \sqrt{k_0^2 \varepsilon_0 - \beta^2}}{k_{z0} + \sqrt{k_0^2 \varepsilon_0 - \beta^2}} \quad (10)$$

For p polarization, the Fresnel coefficient  $r_p$  can be expressed as follows for uniaxial medium whose optical axis is parallel to the  $z$  axis [36,37]

$$r_p = \frac{\varepsilon_0 k_{z0} - \sqrt{k_0^2 \varepsilon_0 - \beta^2} \varepsilon_0 / \varepsilon_E}{\varepsilon_0 k_{z0} + \sqrt{k_0^2 \varepsilon_0 - \beta^2} \varepsilon_0 / \varepsilon_E} \quad (11)$$

For gratings, cross-polarization must be considered and the transmission factor can be determined based on the matrix formulation [57]. Considering the azimuthal angle  $\phi$ , the angle between plane of incidence and the  $x$ - $z$  plane as defined in Fig. 1d, the Fresnel reflection coefficients can be explicitly expressed as follows [58]

$$r_{ss} = \frac{n_{z0}(n_z - n_{z0})(\varepsilon_0 n_z n_{zE} + n_{z0}^2) \sin^2 \phi + \varepsilon_0(n_z - n_{zE})(\varepsilon_0 n_z + n_{z0}) \cos^2 \phi}{n_{z0}(n_z + n_{z0})(\varepsilon_0 n_z n_{zE} + n_{z0}^2) \sin^2 \phi + \varepsilon_0(n_z + n_{zE})(\varepsilon_0 n_z + n_{z0}) \cos^2 \phi} \quad (12)$$

$$r_{pp} = \frac{n_{z0}(n_z + n_{z0})(\varepsilon_0 n_z n_{zE} - n_{z0}^2) \sin^2 \phi + \varepsilon_0(n_z + n_{zE})(\varepsilon_0 n_z - n_{z0}) \cos^2 \phi}{n_{z0}(n_z + n_{z0})(\varepsilon_0 n_z n_{zE} + n_{z0}^2) \sin^2 \phi + \varepsilon_0(n_z + n_{zE})(\varepsilon_0 n_z + n_{z0}) \cos^2 \phi} \quad (13)$$

$$r_{sp} = -r_{ps} = \frac{2\varepsilon_0 n_{z0} n_z (n_{z0} - n_{zE}) \sin \phi \cos \phi}{n_{z0}(n_z + n_{z0})(\varepsilon_0 n_z n_{zE} + n_{z0}^2) \sin^2 \phi + \varepsilon_0(n_z + n_{zE})(\varepsilon_0 n_z + n_{z0}) \cos^2 \phi} \quad (14)$$

where

$$n_z = \sqrt{1 - (\beta/k_0)^2}, \quad n_{z0} = \sqrt{\varepsilon_0 - (\beta/k_0)^2}$$

and

$$n_{zE} = \sqrt{\varepsilon_E - (\beta/k_0)^2} \left[ \cos^2 \phi + (\varepsilon_E/\varepsilon_0) \sin^2 \phi \right]. \quad (15)$$

The expressions given above agree with the formulation given in Rosa et al. [57], except with a sign difference in the cross-polarization terms  $r_{sp}$  and  $r_{ps}$  due to the  $180^\circ$  phase difference of the rotation (azimuthal) angle. The plane of incidence is perpendicular to optical axis when  $\phi = 0^\circ$  and  $180^\circ$ , and parallel to optical axis at  $\phi = 90^\circ$  and  $270^\circ$ . It should be noted that integration over azimuthal angles is necessary since Fresnel's coefficients depend on  $\phi$ , unlike in multilayer and other configurations. When the gratings are aligned as shown in Fig. 1(d), the relationship of azimuthal angles for the two gratings is  $\phi_2 = -\phi_1$ . If there is a relative rotation angle  $\Delta$  between the two gratings, then  $\phi_2 = -\phi_1 + \Delta$ . If the two gratings are identical and aligned,  $\mathbf{R}_1$  and  $\mathbf{R}_2$  are transpose of each other, since  $r_{ss}(-\phi) = r_{ss}(\phi)$ ,  $r_{pp}(-\phi) = r_{pp}(\phi)$ ,  $r_{sp}(-\phi) = -r_{sp}(\phi) = r_{ps}(\phi)$ , and  $r_{ps}(-\phi) = -r_{ps}(\phi) = r_{sp}(\phi)$ . The results have been verified by comparison with Biéhs et al. [17].

### 3. Results and discussions

All the calculations are for room temperature with  $T = 300$  K. Only  $n$ -type D-Si is considered in this work, while similar results

can be obtained for p-type D-Si, though not shown in this work. In most of the calculations, the doping concentration is set to  $N = 10^{20} \text{ cm}^{-3}$ , which will be the default value unless otherwise specified. At this doping concentration,  $\varepsilon_\infty$  can be approximated as a constant of 11.7, and  $\omega_p$  and  $\gamma$  are taken as  $1.08 \times 10^{15} \text{ rad/s}$  and  $9.34 \times 10^{13} \text{ rad/s}$ , respectively [51].

#### 3.1. Near-field thermal radiation between nanostructures

The radiative heat transfer coefficient versus the filling ratio of D-Si for the four nanostructures at a distance  $d = 10$  nm is shown in Fig. 2. The radiative heat transfer coefficient is normalized to that of bulk D-Si in order to show the enhancement or reduction of heat transfer by the nanostructures. Note that the heat transfer coefficient for bulk D-Si at this distance with the same doping level is  $5022 \text{ W/m}^2 \text{ K}$ , which is 820 times the value between two blackbodies (i.e.,  $4\sigma T^3$  where  $\sigma$  is the Stefan-Boltzmann constant). The enhancement of heavily doped Si is due to surface waves [29,43,46]. Fig. 2 suggests that D-SiNWs with  $f = 0.05$  can achieve an enhancement factor of 12.5 over bulk D-Si. With the nanowires, the predicted heat transfer coefficient exceeds  $60,000 \text{ W/m}^2 \text{ K}$  at  $d = 10$  nm, making D-SiNWs very attractive for applications ranging from high-efficiency near-field radiative cooling to local heating. The enhancement over bulk by nanoholes increases with decreasing  $f$  and reaches the maximum of 11.3 times when  $f = 1 - \pi/4$ . For 1D gratings, the calculation is based on  $\Delta = 0^\circ$  unless otherwise specified since the alignment case yields the maximum heat transfer. For 1D gratings, there is a slight enhancement when  $f > 0.2$  and the maximum enhancement is around  $f = 0.4$  with a ratio  $h/h_{\text{bulk}} = 1.19$ . However, the near-field radiative transfer coefficient between two multilayers is always smaller than that of the bulk and increases monotonously with  $f$ . Therefore, multilayer structures are not as effective in terms of enhancing near-field radiative transfer at ambient temperature and at deep submicron gap distances. Similar trends can be obtained for  $d = 100$  nm with reduced heat flux, although the results are not shown here.

In order to see whether the performance achieved with these nanostructures will still hold at different gap distances, relative

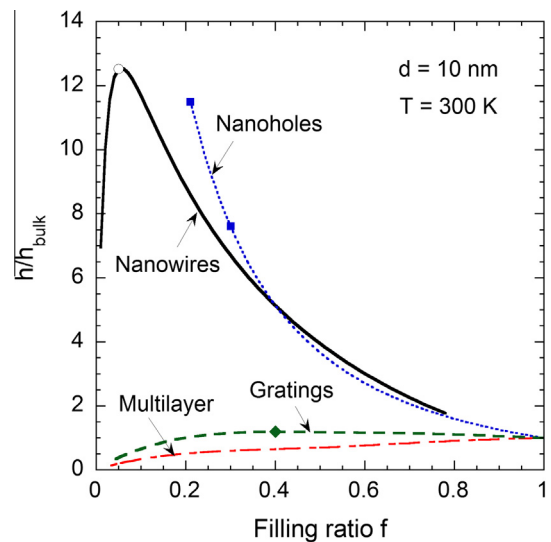


**Fig. 2.** Ratio of the heat transfer coefficient of the nanostructures to bulk doped silicon and a gap distance of 10 nm. For all the nanostructures, the filling ratio refers to the fraction of doped silicon. Note that the minimum filling ratio for nanoholes is  $1 - \pi/4$ , while the maximum filling ratio for nanowires is  $\pi/4$ . The gratings are assumed to be aligned ( $\Delta = 0^\circ$ ) unless otherwise mentioned. In the present study, the temperature of 300 K is used and the doping concentration is set to  $N = 1 \times 10^{20} \text{ cm}^{-3}$  (for  $n$ -type semiconductor) unless otherwise specified.

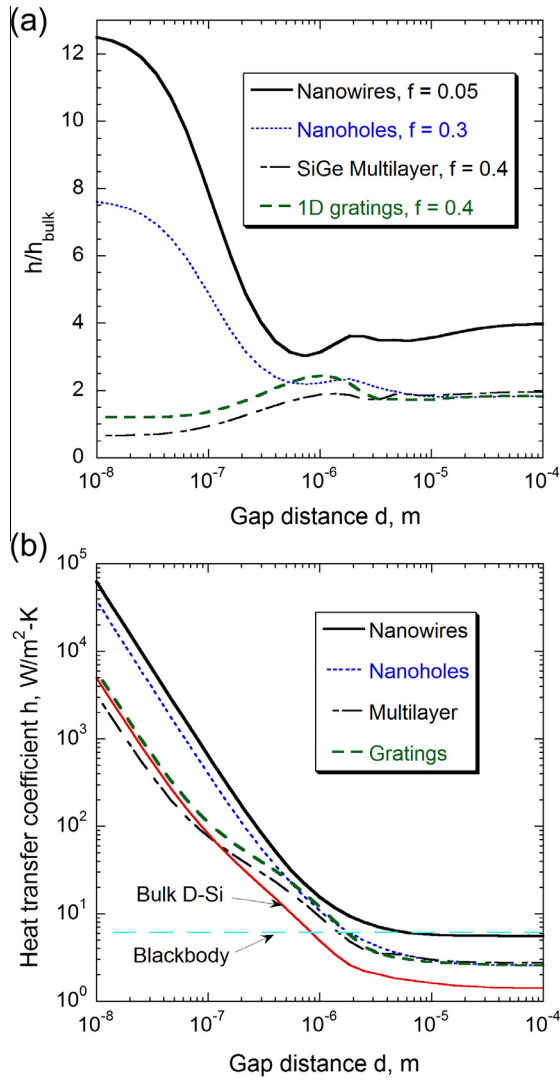


**Fig. 3.** Heat transfer coefficients versus gap distance: (a) the ratio to bulk D-Si for each nanostructure with a selected filling ratio; (b) the absolute  $h$  values of the same nanostructures plotted against those of bulk D-Si and the blackbody limit.

heat transfer coefficient is plotted in Fig. 3a. The filling ratios for nanowires and 1D gratings are taken as the optimized value at  $d = 10$  nm, i.e.,  $f = 0.05$  and  $0.4$ , respectively. For clearer comparison between multilayers and 1D gratings, the filling ratio is also chosen as  $0.4$  for multilayers. The filling ratio of nanoholes is taken as  $0.3$  based on practical consideration to stay away from the physical limitation. It is interesting to note that in the far field, multilayers give slightly higher heat transfer coefficient than nanoholes or 1D gratings. Among all the structures, D-SiNWs result in the largest heat transfer coefficient at any gap distance.

The absolute heat transfer coefficients for all cases shown in Fig. 3a are plotted in Fig. 3b, where the values for bulk D-Si and the far-field blackbody limit are also shown. It can be seen that in the far field, the heat transfer coefficient between D-SiNWs is very close to that between blackbodies due to the good impedance matching and thus low reflectivity [45]. D-SiNWs can yield a super-Planckian behavior when the gap distance is below  $6 \mu\text{m}$ , while for bulk D-Si the heat transfer coefficient exceeds the blackbody limit only when  $d < 0.8 \mu\text{m}$ . Therefore, nanowires can be used to extend the super-Planckian radiative transfer to micrometer gap distances and subsequently may benefit energy harvesting between micrometer gap distances. Meanwhile, nanoholes,

multilayers, and gratings also extend near-field enhancement at greater gap distances though not as high in magnitude as nanowires. This could greatly relieve the fabrication barriers of near-field TPV cells [4–6].

### 3.2. Mechanisms of enhanced near-field radiative transfer

The mechanisms of near-field radiative heat transfer are elucidated to understand the performance of different nanostructures. Both nanowires and nanoholes could achieve an enhancement about one order of magnitude at tens of nanometer distances. The real parts of the anisotropic dielectric functions of D-SiNWs with  $f = 0.05$  and D-SiNHs with  $f = 0.3$  are plotted in Fig. 4. For D-SiNW, the real part of  $\epsilon_x$  is almost a constant close to 1 and independent of wave frequency due to the small filling ratio. The imaginary part (not shown) of  $\epsilon_x$  is generally much smaller than 1. Hence, for electric field perpendicular to the nanowires (ordinary waves), the effective optical properties of the nanowire medium is essentially a dielectric. On the other hand, the effective dielectric function of the nanowires for extraordinary waves is described by

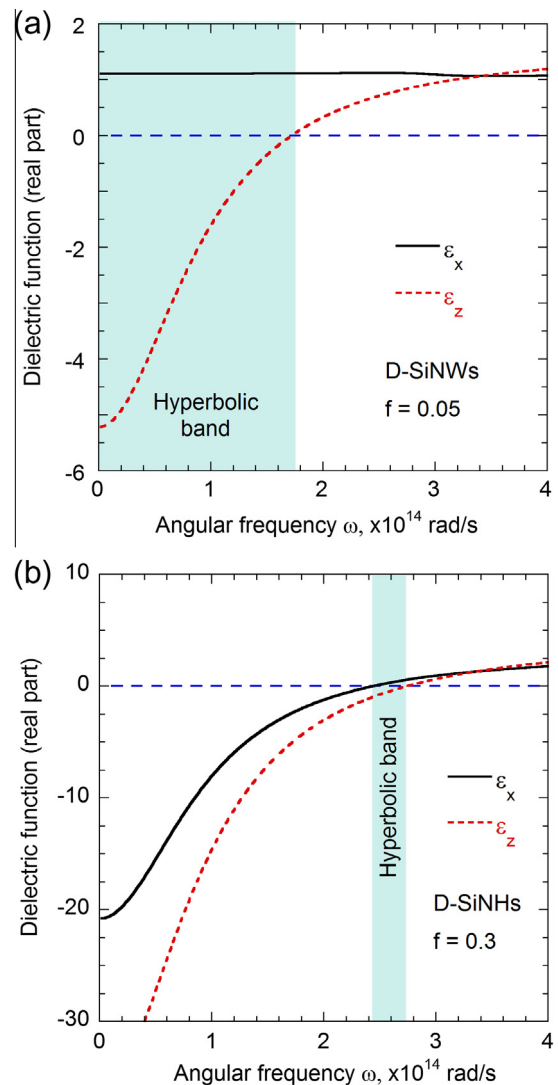


**Fig. 4.** The effective dielectric functions (real part only) for (a) the D-SiNWs at  $f = 0.05$  and (b) D-SiNHs with  $f = 0.3$ . The hyperbolic dispersion (type I) is supported in a broader band at frequencies below  $1.72 \times 10^{14}$  rad/s for D-SiNW and in a narrow band between  $2.44 \times 10^{14}$  rad/s and  $2.74 \times 10^{14}$  rad/s for D-SiNHs as shown by the shaded regions.

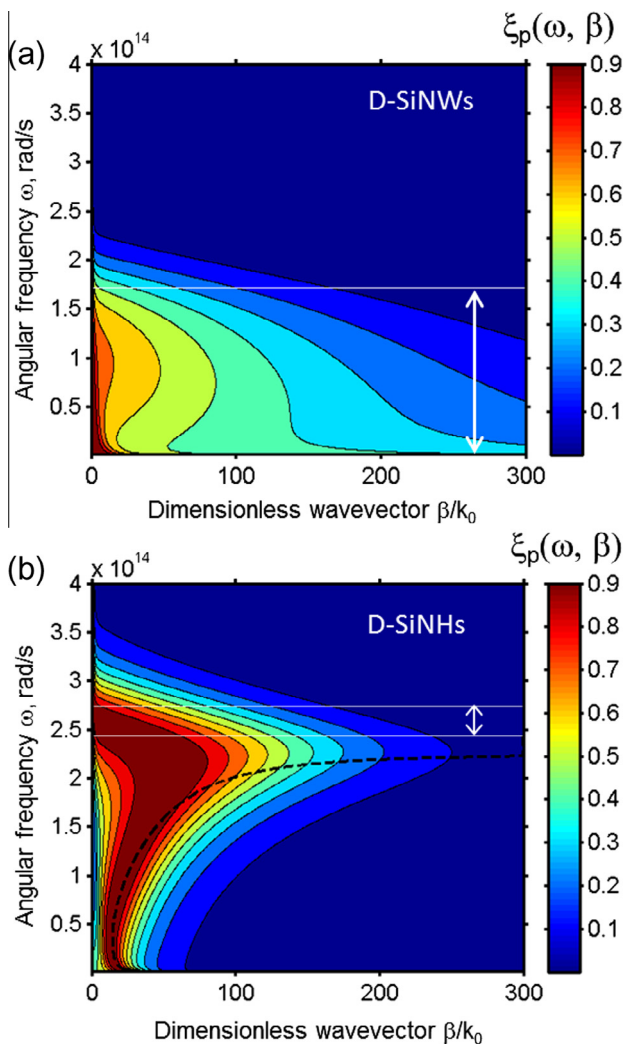
the dilute Drude model and is therefore metallic. When  $\epsilon_x > 0$  and  $\epsilon_z < 0$ , as shown in the shaded region of Fig. 4a, the dispersion relation becomes hyperbolic with negative energy refraction (type I); refer to Cortes et al. [59] for a detailed discussion of the hyperbolic modes and energy refraction in hyperbolic metamaterials. For D-SiNHs, as shown in Fig. 4b, both  $\epsilon_x$  and  $\epsilon_z$  are negative at the frequency region lower than  $2.44 \times 10^{14}$  rad/s. A narrow hyperbolic band, also type I, exists between  $2.44 \times 10^{14}$  rad/s and  $2.74 \times 10^{14}$  rad/s as shown in the shaded region in Fig. 4b.

Fig. 5 displays the contour plots of the transmission factors for p-polarization at  $d = 10$  nm for both D-SiNWs and D-SiNHs corresponding to the dielectric functions shown in Fig. 4. The contribution of s-polarization to near-field radiation is negligible. For D-SiNWs, as shown in Fig. 5a, in the broad hyperbolic band below  $1.72 \times 10^{14}$  rad/s, as delineated by the arrows between the white line and the horizontal axis, both negative refraction and high- $\beta$  propagating waves will be supported. As mentioned previously, the heat transfer coefficient between D-SiNWs at  $d = 10$  nm reaches 12.5 times that between bulk D-Si. This is due to the broad

hyperbolic band that allows photons to tunnel through the vacuum gap at very large  $\beta$  values and in a broad spectral region. In the case of hyperbolic modes, propagating waves exist in the anisotropic medium; on the other hand, surface modes are manifested by evanescent waves in both media.

As shown in Fig. 4b, both  $\epsilon_x$  and  $\epsilon_z$  of D-SiNHs are negative at frequencies lower than  $2.44 \times 10^{14}$  rad/s. Therefore, coupled SPPs could be excited about the frequency corresponding to  $\text{Re}(\sqrt{\epsilon_x \epsilon_z}) = -1$ , which is  $\omega_m = 2.24 \times 10^{14}$  rad/s in this case. The SPP dispersion relation for two metallic uniaxial media separated by a small gap exhibits a high-frequency branch ( $\omega > \omega_m$ ) and a low-frequency branch ( $\omega < \omega_m$ ). Both of the dispersion curves share the same asymptotic limit of  $\omega = \omega_m$  at infinite wavevector (i.e.,  $\beta \rightarrow \infty$ ). For the low-frequency branch, surface charges are symmetric and the magnetic fields at the interface are in phase. The opposite is true for the high-frequency branch. The coupled-SPP dispersion can be obtained by zeroing the denominator of  $\xi_p(\omega, \beta)$ . For the symmetric modes or low-frequency branch, the dispersion relation can be expressed as follows [42,47]

$$k_{z0} = \sqrt{\frac{k_0^2}{\epsilon_x} - \frac{\beta^2}{\epsilon_x \epsilon_z}} \coth\left(\frac{ik_{z0}d}{2}\right) \quad (16)$$



**Fig. 5.** Contour plots of the energy transmission factor for p-polarization  $\xi_p(\omega, \beta)$  of (a) D-SiNWs and (b) D-SiNHs for  $d = 10$  nm, using the dielectric functions shown in Fig. 4. The corresponding hyperbolic bands are indicated between the two horizontal white lines. For D-SiNHs, the SPP resonance frequency is at  $2.24 \times 10^{14}$  rad/s, and the symmetric coupled SPP dispersion is displayed as the black dashed curve. Note that in the proximity limit, the contribution of s-polarization to near-field radiation is negligibly small when either hyperbolic modes or surface modes are excited.

The dispersion relation of the asymmetric modes is written by substituting “tanh” for the “coth” in Eq. (16). For real values of  $\omega$  and  $\beta$ , solution of the SPP dispersion relation exists only when there is no loss. In the case with low loss, damping effect can be included, resulting in a peak broadening. When loss is very high, interpretation becomes difficult. It has been shown that near-field radiative heat transfer can still be enhanced about the surface plasmon frequency  $\omega_m$  for both isotropic and anisotropic materials [27,29,47]. This can also be seen in Fig. 5b where the cutoff wavevector is large near  $\omega_m$ . Note that the cutoff wavevector is defined as the maximum  $\beta$  value beyond which the contribution to near-field heat transfer can be essentially neglected (or is a small percentage of the integral over  $\beta$ ). By finding the minimum in the denominator of  $\xi_p(\omega, \beta)$ , the symmetric coupled-SPP dispersion is obtained and plotted in Fig. 5b as the black dashed curve, which agrees with the contour of transmission factor reasonably well. The asymmetric branch is expected to lie between  $\omega_m$  and the hyperbolic region if there were no loss. However, when loss is considered, there exist no minimum in the denominator of  $\xi_p(\omega, \beta)$  in this region for real values of  $\omega$  and  $\beta$ . The enhancement in  $\xi_p(\omega, \beta)$  in this region mostly comes from the large numerator of  $\xi_p(\omega, \beta)$ . It seems that only the symmetric modes are excited in the considered case. For this reason, the asymmetric dispersion is not shown in Fig. 5b. The contribution of the symmetric modes ( $\omega < \omega_m$ ) to the heat transfer coefficient is 71.5%. The contribution from frequencies ranging from  $2.24 \times 10^{14}$  to  $2.44 \times 10^{14}$  rad/s is 14.2%. Whether the excitation is classified as SPPs or not, evanescent waves and phonon tunneling still exist in this frequency region [23]. Note that hyperbolic modes ( $2.44 \times 10^{14}$  rad/s  $< \omega < 2.74 \times 10^{14}$  rad/s) contribute 10.8% to the heat transfer coefficient. Therefore, coupled SPPs or surface modes are largely responsible for the near-field heat transfer enhancement in D-SiNHs. While coupled-SPP modes can also exist between D-Si, due to the high loss in the bulk material, high  $\xi_p(\omega, \beta)$  occurs at relatively small  $\beta$  values. The cutoff wavevector increases with reducing material loss [27,36]. At the resonance frequency ( $2.88 \times 10^{14}$  rad/s), the imaginary part of the dielectric function of D-Si is nearly twice of  $\text{Im}(\sqrt{\epsilon_0 \epsilon_E})$  at  $2.24 \times 10^{14}$  rad/s. Therefore, the number of contributing modes of low-loss D-SiNHs is much greater than that of D-Si, resulting in a much greater enhancement of near-field thermal radiation.

The effective dielectric functions of D-Si/Ge multilayers with  $f = 0.4$  are shown in Fig. 6a (only the real part). For multilayers,  $\epsilon_x = \epsilon_0$  is governed by dilute Drude model given in Eq. (4a), while

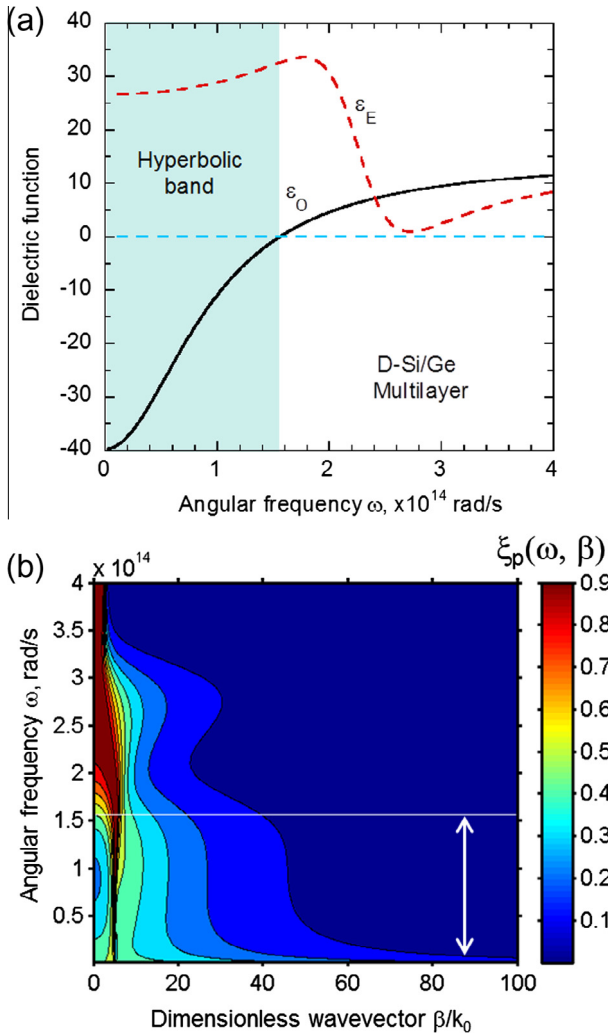


**Fig. 6.** (a) Effective dielectric function of D-Si/Ge multilayers with  $f=0.4$ ; (b) contour plots of the p-polarization transmission factor at  $d=10$  nm for the configuration with two multilayers using the dielectric function shown in (a). The type II hyperbolic band is indicated on both plots at the low frequency region for  $\omega < 1.55 \times 10^{14}$  rad/s.

$\epsilon_z = \epsilon_E$  is governed by the Lorentz model given in Eq. (4b). When  $\epsilon_x < 0$  and  $\epsilon_z > 0$ , the dispersion becomes hyperbolic (type II), as shown in Fig. 6a in the shaded area at frequencies below  $1.55 \times 10^{14}$  rad/s. The p-polarization transmission factor  $\xi_p(\omega, \beta)$  is shown in Fig. 6b and the contribution from s-polarization to heat transfer is negligibly small at nanometer gap distances. In the multilayer configuration, type II hyperbolic materials do not yield negative refraction [59]. Another uniqueness of type II hyperbolic modes is that  $\xi_p(\omega, \beta)$  becomes non-trivial only when  $\beta$  is greater than the critical wavevector  $k_{cr} = k_0 \sqrt{\epsilon_E}$  [54]. When  $\beta > k_{cr}$ , propagating hyperbolic modes will be supported with a high transmission factor in a broadband region independent of type I or type II [42]. Therefore, the spectral heat flux can be enhanced over bulks in a broad band due to the high transmission factor for large  $\beta$  in either type of hyperbolic mode. Nevertheless, due to losses, the transmission factor decreases much faster for multilayer structure than for nanowires or nanoholes at large  $\beta$  values. Furthermore, in the high frequency region outside the hyperbolic band, especially near the surface resonance frequency of D-Si ( $2.90 \times 10^{14}$  rad/s), the spectral flux between multilayered structures is much less than that between bulks. The overall effect is that the enhancement of

heat transfer in the low-frequency region cannot compensate for the reduction in the high-frequency region, resulting in a net reduction of radiative heat transfer coefficient over bulk D-Si. The ratio  $h/h_{bulk}$  is 0.65 for multilayers with  $f=0.4$ . Nevertheless, with increasing gap distance, the heat transfer coefficient for bulk D-Si decreases faster than that for multilayers as shown in Fig. 3. For multilayers with  $f=0.4$ ,  $h > h_{bulk}$  when  $d$  exceeds 120 nm and  $h \approx 2h_{bulk}$  in the far field.

The heat transfer mechanisms between gratings are more complicated. For nonmagnetic materials, s-polarized waves generally cannot excite surface modes except for the case with negative-permeability metamaterials [24,60]. However, for 1D gratings when the azimuthal angle is nonzero, s-polarized incident waves can also excite SPPs since there will be a magnetic field along the grooves and a wavevector component perpendicular to the grooves [61]. When the gratings are homogenized as an anisotropic medium, the nanoscale radiative transfer is governed by the transmission factor and more specifically by Fresnel's reflection coefficients when  $\beta \gg k_0$ . A close examination of Eq. (14) suggests that the cross-polarization terms are negligibly small when  $\beta \gg k_0$ . Therefore, polarization coupling will contribute little to the radiative heat transfer in the deep submicron region. Furthermore, regard-

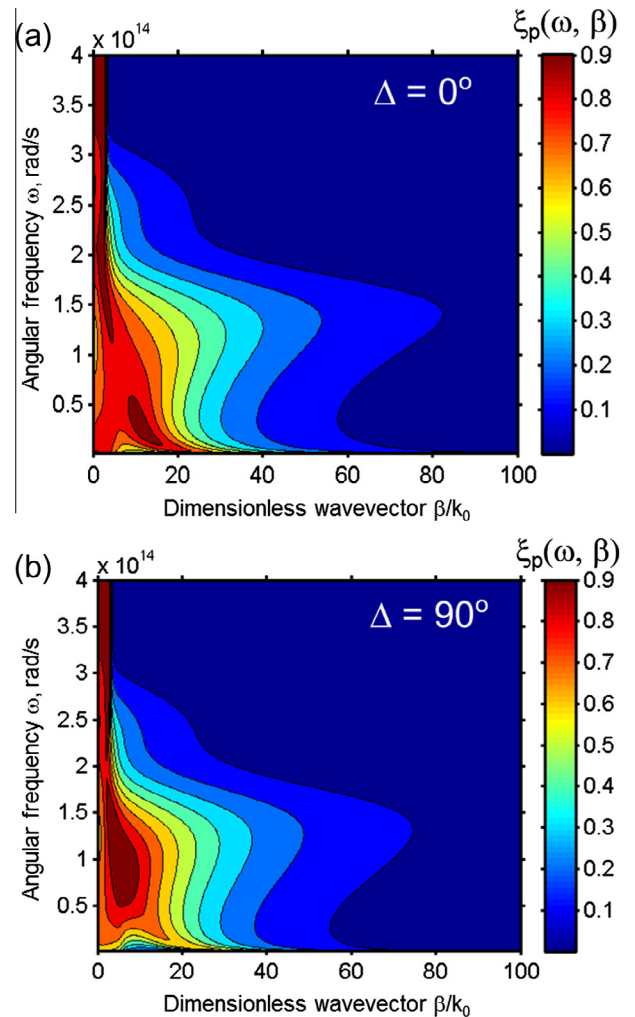


**Fig. 7.** Contours of the transmission factor for p-polarization integrated over the azimuthal angle with  $d=10$  nm between aligned 1D gratings: (a) parallel aligned gratings with a relative rotation angle  $\Delta = 0^\circ$ ; (b) perpendicularly aligned gratings with  $\Delta = 90^\circ$ . The contributions from s-polarization and polarization coupling to near-field radiation are negligible for large wavevectors ( $\beta/k_0 \gg 1$ ).

less of the azimuthal angle,  $\text{Im}(r_{ss})$  quickly approaches zero as  $\beta/k_0$  increases. Hence, the contribution of s-polarization to nanoscale radiation is also negligible. Fig. 7 shows the contours of the p-polarization transmission factor for  $f=0.4$  and  $d=10$  nm integrated over the azimuthal angle for aligned ( $\Delta=0^\circ$ ) and crossed ( $\Delta=90^\circ$ ) gratings, respectively. The shapes for  $\Delta=0^\circ$  and  $90^\circ$  are similar with slightly larger transmission factors and cutoff wavevectors for the aligned case. Note that the ordinary and extraordinary dielectric functions are the same as shown in Fig. 6a for multilayers, except that for gratings  $\epsilon_z = \epsilon_0$  and  $\epsilon_x$  and  $\epsilon_y$  depends on the rotation angle. Compared with Fig. 6b, gratings can increase the transmission factor toward large  $\beta$  values over multilayers, especially near the frequency of  $1.5 \times 10^{14}$  rad/s. The reason is due to the large  $\text{Im}(r_{pp})$  and subsequently larger transmission coefficients ( $\xi_p$ ) for gratings. Therefore, the near-field radiative transfer of gratings is more than those of bulk D-Si and multilayers.

The relative heat transfer coefficient as a function of relative rotation angle of the gratings is shown in Fig. 8 for  $d=10$  nm and  $f=0.4$ . It can be seen that  $h$  monotonically decreases as  $\Delta$  is increased from  $0^\circ$  to  $90^\circ$  due to symmetry breaking. It has been proposed that 1D gratings may potentially be used as non-contact thermal modulators [17]. Note that the maximum modification with D-Si/Ge multilayer is about 10%, much lower than those with Au and SiC [17]; this is presumably due to the large scattering rate in D-Si.

3.3. Effect of doping concentration

Since D-SiNWs and D-SiNHs can provide the greatest enhancement of near-field heat flux, the effect of doping concentration for these structures is examined. Fig. 9 shows the contours of the heat transfer coefficients at  $d=10$  nm in terms of the filling ratio and doping concentration. The doping concentration  $N$  is varied from  $10^{19}$  to  $10^{21}$   $\text{cm}^{-3}$ . For D-SiNWs, the filling ratio  $f$  is varied from 0.01 to  $\pi/4$ , which is the upper limit. The maximum heat transfer coefficient exceeds  $60,000 \text{ W/m}^2 \text{ K}$  in the elliptical region centered around  $f=0.04$  and  $N=5 \times 10^{20} \text{ cm}^{-3}$ . For D-SiNHs,  $f$  is varied from  $1 - \pi/4$  (about 0.215) to 1 (i.e., bulk D-Si). For any given doping concentration, decreasing the filling ratio reduces loss and increases the heat transfer rate since the cutoff wavevector will increase [37]. Interestingly, the maximum heat transfer coefficient is near  $N=4 \times 10^{19} \text{ cm}^{-3}$ , with a value close to  $70,000 \text{ W/m}^2 \text{ K}$ . It

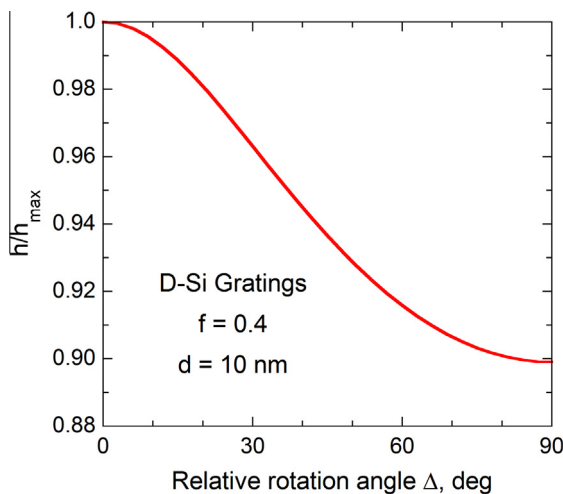


Fig. 8. The near-field heat transfer coefficient for  $d=10$  nm as a function of the relative rotation angle of the gratings when  $f=0.4$ . The maximum occurs when there is no relative rotation between the gratings (parallel case) and the minimum occurs when the gratings are perpendicular to each other.

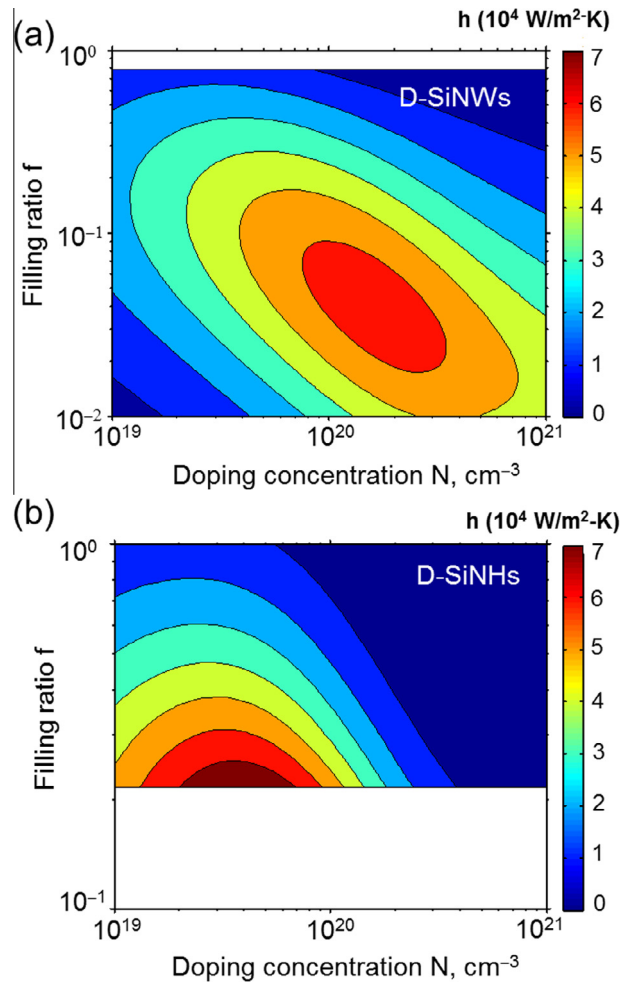


Fig. 9. Contour plots of the heat transfer coefficient for (a) D-SiNWs and (b) D-SiNHs in terms of the doping concentration and filling ratio.

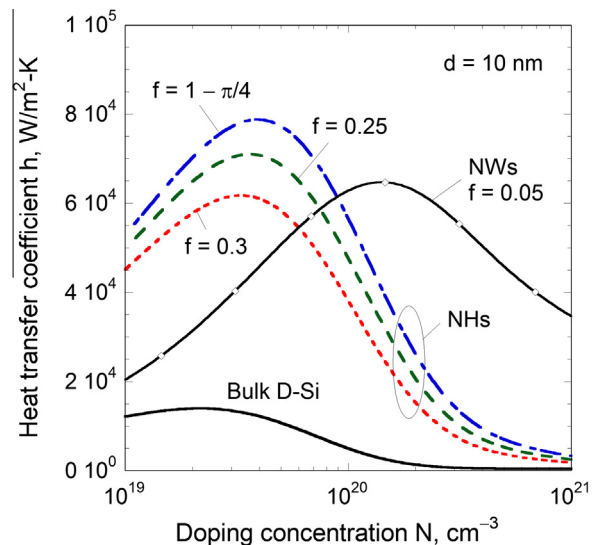


Fig. 10. Heat transfer coefficient for D-SiNWs and D-SiNHs for selected filling ratios, as well as that of bulk D-Si, versus doping concentration.

should be noted that this value is about 22% of the upper limit for hyperbolic modes without considering dispersion or loss [37]. In Fig. 10,  $h$  for D-SiNWs with  $f=0.05$  and D-SiNHs with several  $f$

values is plotted versus the doping concentration. The heat transfer coefficient for bulk D-Si is also shown for comparison. In terms of the absolute value of  $h$ , nanoholes can outperform nanowires to achieve the maximum heating or cooling at tens-of-nanometer distances when the doping concentration and filling ratio are optimized. On the other hand, both D-SiNWs and D-SiNHs can achieve a heat flux enhancement by an order of magnitude over bulk D-Si when  $N \approx 1 \times 10^{20} \text{ cm}^{-3}$ . Similar trends hold for different gap distances, such as  $d = 100 \text{ nm}$ , though not shown here. It should be reminded that main cause of the large enhancement is due to the hyperbolic modes in D-SiNWs and low-loss surface modes in D-SiNHs.

#### 4. Conclusions

Different practically achievable nanostructures based on doped silicon are investigated for enhancement of near-field radiative heat transfer at ambient temperature. Three out of the four configurations (D-SiNWs, D-SiNHs, and D-Si gratings) can enhance radiative heat transfer over bulk D-Si from tens of nanometers to the far field. The fourth configuration, multilayers, can also give a radiative heat flux that is almost twice as large as that between bulks in the far field. It is predicted that D-SiNWs and D-SiNHs can provide an enhancement over bulks by more than one order of magnitude in the deep submicron gap region, due to broadband hyperbolic modes and low-loss surface modes, respectively. These two configurations can be designed with optimal doping and geometrical criteria. The mechanism of near-field radiative transfer between gratings made of D-Si and Ge is also investigated. It is found that s-polarization and polarization coupling are negligible for near-field heat transfer analysis at deep submicron distances. Thus, the dominating mechanism for near-field radiation between gratings is the same as for other nonmagnetic materials; that is, the nontrivial transmission coefficients at large transverse wavevectors are enabled by p-polarized waves. The alignment between gratings has a relatively small effect on the near-field radiative transfer for D-Si/Ge gratings. The analysis and methodology presented in this work may benefit the design of nanostructures in applications such as more efficient non-contact thermal management and microgap thermophotovoltaics.

#### Acknowledgments

The support from the Department of Energy (DE-FG02-06ER46343) for XLL and that from the National Science Foundation (CBET-1235975) for RZZ and ZMZ are gratefully acknowledged.

#### References

- [1] M. Whale, E. Cravalho, Modeling and performance of microscale thermophotovoltaic energy conversion devices, *IEEE Trans. Energy Convers.* 17 (2002) 130–142.
- [2] A. Narayanaswamy, G. Chen, Surface modes for near field thermophotovoltaics, *Appl. Phys. Lett.* 82 (2003) 3544–3546.
- [3] M. Laroche, R. Carminati, J.J. Greffet, Near-field thermophotovoltaic energy conversion, *J. Appl. Phys.* 100 (2006) 063704.
- [4] K. Park, S. Basu, W.P. King, Z.M. Zhang, Performance analysis of near-field thermophotovoltaic devices considering absorption distribution, *J. Quant. Spectrosc. Radiat. Transfer* 109 (2008) 305–316.
- [5] S. Basu, Z.M. Zhang, C.J. Fu, Review of near-field thermal radiation and its application to energy conversion, *Int. J. Energy Res.* 33 (2009) 1203–1232.
- [6] M. Francoeur, R. Vaillon, M.P. Mengüç, Thermal impacts on the performance of nanoscale-gap thermophotovoltaic power generators, *IEEE Trans. Energy Convers.* 26 (2011) 686–698.
- [7] O. Ilic, M. Jablan, J.D. Joannopoulos, I. Celanovic, M. Soljačić, Overcoming the black body limit in plasmonic and graphene near-field thermophotovoltaic systems, *Opt. Express* 20 (2012) A366–384.
- [8] R. Messina, P. Ben-Abdallah, Graphene-based photovoltaic cells for near-field thermal energy conversion, *Sci. Rep.* 3 (2013) 1383.
- [9] K. Dransfeld, J. Xu, The heat transfer between a heated tip and a substrate: fast thermal microscopy, *J. Microsc.* 152 (1988) 35–42.
- [10] A. Kittel, W. Müller-Hirsch, J. Parisi, S.-A. Biehs, D. Reddig, M. Holthaus, Near-field heat transfer in a scanning thermal microscope, *Phys. Rev. Lett.* 95 (2005) 224301.
- [11] Y. De Wilde, F. Formanek, R. Carminati, B. Gralak, P.A. Lemoine, K. Joulain, J.-P. Mulet, Y. Chen, J.-J. Greffet, Thermal radiation scanning tunnelling microscopy, *Nature* 444 (2006) 740–743.
- [12] A.C. Jones, M.B. Raschke, Thermal infrared near-field spectroscopy, *Nano Lett.* 12 (2012) 1475–1481.
- [13] C.R. Otey, W.T. Lau, S. Fan, Thermal rectification through vacuum, *Phys. Rev. Lett.* 104 (2010) 154301.
- [14] S. Basu, M. Francoeur, Near-field radiative transfer based thermal rectification using doped silicon, *Appl. Phys. Lett.* 98 (2011) 113106.
- [15] H. Iizuka, S. Fan, Rectification of evanescent heat transfer between dielectric-coated and uncoated silicon carbide plates, *J. Appl. Phys.* 112 (2012) 024304.
- [16] L.P. Wang, Z.M. Zhang, Thermal rectification enabled by near-field radiative heat transfer between intrinsic silicon and other materials, *Nanoscale Microscale Thermophys. Eng.* 17 (2013) 337–348.
- [17] S.-A. Biehs, F.S.S. Rosa, P. Ben-Abdallah, Modulation of near-field heat transfer between two gratings, *Appl. Phys. Lett.* 98 (2011) 243102.
- [18] L. Cui, Y. Huang, J. Wang, K.-Y. Zhu, Ultrafast modulation of near-field heat transfer with tunable metamaterials, *Appl. Phys. Lett.* 102 (2013) 053106.
- [19] P.J. van Zwol, L. Ranno, J. Chevrier, Tuning near field radiative heat flux through surface excitations with a metal insulator transition, *Phys. Rev. Lett.* 108 (2012) 234301.
- [20] B. Guha, C. Otey, C.B. Poitras, S. Fan, M. Lipson, Near-field radiative cooling of nanostructures, *Nano Lett.* 12 (2012) 4546–4550.
- [21] A. Nemilentsau, S.V. Rotkin, Optimization of nanotube thermal interconnects for near-field radiative heat transport, *Appl. Phys. Lett.* 101 (2012) 063115.
- [22] M. Tschikin, S.-A. Biehs, F.S.S. Rosa, P. Ben-Abdallah, Radiative cooling of nanoparticles close to a surface, *Eur. Phys. J. B* 85 (2012) 233–240.
- [23] C. Fu, Z.M. Zhang, Nanoscale radiation heat transfer for silicon at different doping levels, *Int. J. Heat Mass Transfer* 49 (2005) 1703–1718.
- [24] Z.M. Zhang, *Nano/Microscale Heat Transfer*, McGraw-Hill, New York, 2007.
- [25] K. Park, Z.M. Zhang, Fundamentals and applications of near-field radiative energy transfer, *Front. Heat Mass Transfer* 4 (2013) 013001.
- [26] K. Joulain, J.-P. Mulet, F. Marquier, R. Carminati, J.-J. Greffet, Surface electromagnetic waves thermally excited: radiative heat transfer, coherent properties and Casimir forces revisited in the near field, *Surf. Sci. Rep.* 57 (2005) 59–112.
- [27] X.J. Wang, S. Basu, Z.M. Zhang, Parametric optimization of dielectric functions for maximizing nanoscale radiative transfer, *J. Phys. D: Appl. Phys.* 42 (2009) 245403.
- [28] M. Francoeur, M.P. Mengüç, R. Vaillon, Near-field radiative heat transfer enhancement via surface phonon polaritons coupling in thin films, *Appl. Phys. Lett.* 93 (2008) 043109.
- [29] S. Basu, B.J. Lee, Z.M. Zhang, Near-Field radiation calculated with an improved dielectric function model for doped silicon, *J. Heat Transfer* 132 (2010) 023302.
- [30] L. Hu, A. Narayanaswamy, X.Y. Chen, G. Chen, Near-field thermal radiation between two closely spaced glass plates exceeding Planck's blackbody radiation law, *Appl. Phys. Lett.* 92 (2008) 133106.
- [31] S. Shen, A. Narayanaswamy, G. Chen, Surface phonon polaritons mediated energy transfer between nanoscale gaps, *Nano Lett.* 9 (2009) 2909–2913.
- [32] E. Rousseau, A. Siria, G. Jourdan, S. Volz, F. Comin, J. Chevrier, J.J. Greffet, Radiative heat transfer at the nanoscale, *Nat. Photonics* 3 (2009) 514–517.
- [33] R.S. Ottens, V. Quetschke, S. Wise, A.A. Alemi, R. Lundock, G. Mueller, D.H. Reitze, D.B. Tanner, B.F. Whiting, Near-field radiative heat transfer between macroscopic planar surfaces, *Phys. Rev. Lett.* 107 (2011) 014301.
- [34] T. Kralik, P. Hanzelka, M. Zobac, V. Musilova, T. Fort, M. Horak, Strong near-field enhancement of radiative heat transfer between metallic surfaces, *Phys. Rev. Lett.* 109 (2012) 224302.
- [35] S. Shen, Experimental studies of radiative heat transfer between bodies at small separations, *Annu. Rev. Heat Transfer* 16 (2013) 327–343.
- [36] S.-A. Biehs, P. Ben-Abdallah, F.S.S. Rosa, K. Joulain, J.J. Greffet, Nanoscale heat flux between nanoporous materials, *Opt. Express* 19 (2011) A1088–A1103.
- [37] S.-A. Biehs, M. Tschikin, P. Ben-Abdallah, Hyperbolic metamaterials as an analog of a blackbody in the near field, *Phys. Rev. Lett.* 109 (2012) 104301.
- [38] S.-A. Biehs, M. Tschikin, R. Messina, P. Ben-Abdallah, Super-Planckian near-field thermal emission with phonon-polaritonic hyperbolic metamaterials, *Appl. Phys. Lett.* 102 (2013) 131106.
- [39] M. Tschikin, S.-A. Biehs, R. Messina, P. Ben-Abdallah, On the limits of the effective description of hyperbolic materials in the presence of surface waves, *J. Opt.* 15 (2013) 105101.
- [40] Y. Guo, C.L. Cortes, S. Molesky, Z. Jacob, Broadband super-Planckian thermal emission from hyperbolic metamaterials, *Appl. Phys. Lett.* 101 (2012) 131106.
- [41] Y. Guo, Z. Jacob, Thermal hyperbolic metamaterials, *Opt. Express* 21 (2013) 15014–15019.
- [42] X.L. Liu, Z.R. Zhang, Z.M. Zhang, Near-field thermal radiation between hyperbolic metamaterials: graphite and carbon nanotubes, *Appl. Phys. Lett.* 103 (2013) 213102.
- [43] E. Rousseau, M. Laroche, J.-J. Greffet, Radiative heat transfer at nanoscale: closed-form expression for silicon at different doping levels, *J. Quant. Spectrosc. Radiat. Transfer* 111 (2010) 1005–1014.

- [44] S.-A. Biehs, E. Rousseau, J.-J. Greffet, Mesoscopic description of radiative heat transfer at the nanoscale, *Phys. Rev. Lett.* 105 (2010) 234301.
- [45] X.L. Liu, L.P. Wang, Z.M. Zhang, Wideband tunable omnidirectional infrared absorbers based on doped-silicon nanowire arrays, *J. Heat Transfer* 135 (2013) 061602.
- [46] J. Shi, P. Li, B. Liu, S. Shen, Tuning near field radiation by doped silicon, *Appl. Phys. Lett.* 102 (2013) 183114.
- [47] S. Basu, L. Wang, Near-field radiative heat transfer between doped silicon nanowire arrays, *Appl. Phys. Lett.* 102 (2013) 053101.
- [48] X.L. Liu, Z.M. Zhang, Metal-free low-loss negative refraction, *Appl. Phys. Lett.* 103 (2013) 103101.
- [49] Z. Huang, N. Geyer, P. Werner, J. de Boor, U. Gösele, Metal-assisted chemical etching of silicon: a review, *Adv. Mater.* 23 (2011) 285–308.
- [50] Z.M. Zhang, H. Ye, Measurement of radiative properties of engineered micro-/nanostructures, *Annu. Rev. Heat Transfer* 16 (2013) 345–396.
- [51] S. Basu, B.J. Lee, Z.M. Zhang, Infrared radiative properties of heavily doped silicon at room temperature, *J. Heat Transfer* 132 (2010) 023301.
- [52] I.S. Nefedov, C.R. Simovski, Giant radiation heat transfer through micron gaps, *Phys. Rev. B* 84 (2011) 195459.
- [53] A.A. Orlov, P.M. Voroshilov, P.A. Belov, Y.S. Kivshar, Engineered optical nonlocality in nanostructured metamaterials, *Phys. Rev. B* 84 (2011) 045424.
- [54] O. Kidwai, S.V. Zhukovsky, J.E. Sipe, Effective-medium approach to planar multilayer hyperbolic metamaterials: strengths and limitations, *Phys. Rev. A* 85 (2012) 053842.
- [55] G.L. Carr, S. Perkowitz, D.B. Tanner, Far-infrared properties of inhomogeneous materials, in: W.J. Button (Ed.), *Infrared and Millimeter Waves*, vol. 13, Academic, 1985, pp. 171–263.
- [56] C.F. Bohren, D.R. Huffman, *Absorption and Scattering of Light by Small Particles*, Wiley, New York, 1983.
- [57] F.S.S. Rosa, D.A.R. Dalvit, P.W. Milonni, Casimir interactions for anisotropic magnetodielectric metamaterials, *Phys. Rev. A* 78 (2008) 032117.
- [58] C.G. Malone, B.I. Choi, M.I. Flik, E.G. Cravalho, Spectral emissivity of optically anisotropic solid media, *J. Heat Transfer* 115 (1993) 1021–1028.
- [59] C.L. Cortes, W. Newman, S. Molesky, Z. Jacob, Quantum nanophotonics using hyperbolic metamaterials, *J. Opt.* 14 (2012) 063001.
- [60] Z. Zheng, Y. Xuan, Theory of near-field radiative heat transfer for stratified magnetic media, *Int. J. Heat Mass Transfer* 54 (2011) 1101–1110.
- [61] F. Marquier, M. Laroche, R. Carminati, J.-J. Greffet, Anisotropic polarized emission of a doped silicon lamellar grating, *J. Heat Transfer* 129 (2007) 11–16.